

Contrast of 10–20-day and 30–60-day intraseasonal SST propagation during summer and winter over the South China Sea and western North Pacific

Xi Cao¹ · Renguang Wu^{1,2} · Shangfeng Chen¹

Received: 21 December 2015 / Accepted: 16 April 2016 / Published online: 23 April 2016
© Springer-Verlag Berlin Heidelberg 2016

Abstract This study documents the structure and propagation of intraseasonal sea surface temperature (SST) variations and relative contribution of surface latent heat flux and shortwave radiation to the SST propagation in the South China Sea (SCS) and western North Pacific (WNP) regions. The emphasis is on the contrast of intraseasonal SST propagation between summer and winter and between 10–20-day and 30–60-day time scales. The dominant SST pattern during summer displays a tilted southwest–north-east band from the SCS to the subtropical WNP on both time scales, but with a larger value in the subtropical WNP on the 10–20-day time scale and in the SCS on the 30–60-day time scale. The dominant SST pattern during winter resembles that during summer, but with a larger value in the SCS. In summer, the SST anomalies show obvious northwestward and northward propagations in the SCS–WNP region on the 10–20-day and 30–60-day time scales, respectively. The cloud–radiation effect is a dominant factor for the SST propagation on both time scales in the SCS–WNP region, with a supplementary effect from the wind–evaporation effect on the 10–20-day time scale. In winter, the SST anomalies show southward propagation on both time scales in the SCS, while the southward propagation in the WNP is weak and confined to the subtropics

on the 10–20-day time scale. The wind–evaporation effect makes a larger contribution to the SST propagation than the cloud–radiation effect on both time scales in the SCS–WNP region.

Keywords Intraseasonal SST propagation · Surface heat flux contribution · Summer and winter · 10–20-Day and 30–60-day time scales

1 Introduction

The intraseasonal oscillation (ISO) is one of the most significant signals over the tropical Indian Ocean, the South China Sea (SCS), and the tropical western North Pacific (WNP) regions. The pioneering work by Madden and Julian (1971) first detected the ISO signal in the zonal wind field. Large intraseasonal variability in the SST field has also been detected in the above regions via buoy observations and satellite retrievals (Lau and Sui 1997; Sengupta et al. 2001; Vecchi and Harrison 2002; Xie et al. 2007; Wu 2010). The connection between intraseasonal sea surface temperature (SST) variations and atmospheric ISOs has been confirmed by previous studies (Woolnough et al. 2000; Kemball-Cook and Wang 2001; Fu et al. 2003; Wu et al. 2008; Roxy and Tanimoto 2012; Wu 2016).

The eastward propagation of the atmospheric ISOs along the equator is a prominent feature (e.g., Wang and Rui 1990). During boreal summer, the atmospheric ISOs display northward or northeastward propagation over the Indian Ocean region (e.g., Yasunari 1981; Jiang et al. 2004; Chou and Hsueh 2010) and northward or northwestward propagation over the WNP region (e.g., Wang and Wu 1997; Hsu and Weng 2001; Hsu et al. 2004; Kajikawa and Yasunari 2005). During boreal winter, the prevailing

✉ Renguang Wu
renguang@mail.iap.ac.cn

¹ Center for Monsoon System Research, Institute of Atmospheric Physics, Chinese Academy of Sciences, Building 40, Huayanli, Beichen West Road, Chaoyang District, Beijing, China

² State Key Laboratory of Numerical Modeling for Atmospheric Sciences and Geophysical Fluid Dynamics, Institute of Atmospheric Physics, Chinese Academy of Sciences, Beijing, China

eastward propagation is accompanied by poleward propagation over the off-equatorial regions of the tropical Indo-western Pacific Ocean (e.g., Hsu 1996; Wheeler and Kiladis 1999; Zhang 2005). Although large intraseasonal SST variations have been revealed, the propagation of intraseasonal SST variations is not yet well understood. It is important to understand the formation and propagation of intraseasonal SST variations and their interaction with atmospheric ISOs, which will help improve our understanding of the propagation and prediction of ISOs in the atmosphere.

Studies indicated that the intraseasonal SST variations in the SCS are associated with atmospheric wind and surface heat flux changes (Gao and Zhou 2002; Xie et al. 2007; Wu et al. 2008; Wu and Chen 2015; Wu et al. 2015; Wu 2016). Most previous studies are concerned with intraseasonal SST variations during boreal summer, with relatively few studies about intraseasonal SST variations during boreal winter. Gao and Zhou (2002) noted different characteristics of the 30–90-day intraseasonal SST variations in the SCS between summer and winter. In boreal summer, the intraseasonal SST perturbations display a zonal distribution and a northeastward propagation, which are related to zonal wind and convection variations. By contrast, in boreal winter, the intraseasonal SST perturbations are localized in the SCS, which is primarily associated with meridional wind variations. Wu and Chen (2015) detected a southward propagation of the East Asian winter monsoon-related surface wind speed and latent heat flux anomalies on the 10–60-day time scale in the SCS, followed by a similar propagation of intraseasonal SST anomalies. Wu (2016) indicated that the southward propagation of SST anomalies on the 10–30-day time scale is coupled with surface wind and latent heat flux anomalies. One issue is whether there are important differences in the SST propagation during boreal summer and winter in the SCS and the WNP regions.

As demonstrated by previous studies (e.g., Fukutomi and Yasunari 1999; Annamalai and Slingo 2001; Kikuchi and Wang 2009), there are two prominent atmospheric ISOs. One is on the 10–20-day time scale and the other is on the 30–60-day time scale. Some differences have been documented in the structure between the two ISOs (Kajikawa and Yasunari 2005; Mao and Chan 2005). One question is how the distribution and evolution of intraseasonal SST perturbations are affected differently by the atmospheric ISOs on the two time scales. A difference in the distribution of high correlation between SST and surface heat flux variations in summer was identified by Ye and Wu (2015). On the 10–20-day time scale, the SST and surface heat flux variations tend to be highly correlated along a southwest–northeast band extending from the SCS to the subtropical WNP. In comparison, on the 30–60-day time scale, the high correlation region features a broad eastward extension from

the SCS to the tropical WNP. The purpose of the present study is to compare the intraseasonal SST propagation on the 10–20-day and 30–60-day time scales and its relation to surface heat flux variations during summer and winter over the SCS and the WNP. Understanding this issue will improve our knowledge regarding the factors for the propagation of intraseasonal SST signals and air–sea coupling on the intraseasonal time scales.

The relationship between intraseasonal SST and surface heat flux variations in the SCS and WNP regions has been addressed by a few previous studies (Duvel and Vialard 2007; Wu et al. 2008; Wu 2010; Roxy and Tanimoto 2012; Wu and Chen 2015; Ye and Wu 2015). These previous studies either focused on intraseasonal variations in a specific season or did not distinguish specifically the time scales of intraseasonal variations. The present study distinguishes from these previous studies in the separation of two intraseasonal time scales and/or the comparison between summer and winter. Recently, Wu et al. (2015) compared the co-variations of SST and surface heat flux between the two intraseasonal time scales and between summer and winter. Their analyses are limited to local relationship. The present study contrasts the propagation of intraseasonal SST anomalies and the effects of surface heat fluxes between summer and winter and between the 10–20-day and 30–60-day time scales. Moreover, the present study compares the relative contributions of surface latent heat flux and shortwave radiation to the propagation of intraseasonal SST anomalies.

In the following, we describe the data and methods in Sect. 2. Section 3 presents the dominant pattern of intraseasonal SST variations and associated variations of surface heat flux, wind, and rain over the SCS and the WNP. In Sect. 4, we compare the propagation of intraseasonal SST anomalies and the relative contributions of surface latent heat flux and shortwave radiation. A summary and discussion are presented in Sect. 5.

2 Data and methods

The SST, rain rate, and cloud liquid water used in the present study are derived from data gathered using the Tropical Rainfall Measuring Mission (TRMM) Microwave Imager (TMI) (Wentz et al. 2000). The TMI data set is available on $0.25^\circ \times 0.25^\circ$ grids starting from January 1998, which can be downloaded from <http://www.remss.com/missions/tmi>. The original TMI data have missing values and have been converted to $1^\circ \times 1^\circ$ grids. The present analysis uses a 3-day running mean.

The present study uses the TropFlux that provides daily surface latent heat flux, shortwave radiation, and surface wind speed at 10 m (Kumar et al. 2012). This data set is on

$1^\circ \times 1^\circ$ grids and available from 1979. The TropFlux data are downloaded from <http://www.incois.gov.in/tropflux/overview.html>. Note that positive value of latent heat flux and shortwave radiation means that the energy transfers from the atmosphere to ocean.

The daily surface zonal and meridional winds used in the present analysis are derived from the National Centers for Environmental Prediction (NCEP)-Department of Energy reanalysis 2 (Kanamitsu et al. 2002). They are available on T62 Gaussian grids from 1979 and obtained by anonymous ftp at <ftp://ftp.cdc.noaa.gov/>.

The present study separates the intraseasonal variations on the 10–20-day and 30–60-day time scales. Following the method of Wu (2010) and Wu et al. (2015), the ISO on the 10–20-day time scale is obtained by a 9-day running mean minus a 21-day running mean, and that on the 30–60-day time scale is obtained by a 29-day running mean minus a 61-day running mean. We analyze the variations and relationship in boreal summer and winter separately. In this study, the boreal summer refers to the months from May to September (MJJAS for brevity), and the boreal winter refers to the months from November to the following March (NDJFM for brevity). The analysis period is from 1998 to 2012 for MJJAS and from 1998/1999 to 2011/2012 for NDJFM when all the variables are available.

This study is concerned with intraseasonal SST variations in the SCS and WNP regions. An empirical orthogonal function (EOF) analysis is applied to get the dominant spatial and temporal structures of the 10–20-day and 30–60-day intraseasonal SST variations during boreal summer and winter, respectively. To detect the propagating feature of intraseasonal SST variations, a lead and lag regression analysis is performed with respect to the principle component (PC) of the leading EOF modes.

The statistical significance of correlation is assessed using the two-sided Student's t test. Following Ye and Wu (2015), the effective degree of freedom (DOF) is estimated by $DOF = TND/MD * YD - 2$, where TND is the total number of days during MJJAS (153-day) or during NDJFM (151-day or 152-day), MD is the medium value of the ISO time period (15-day for the 10–20-day ISO and 45-day for 30–60-day ISO) and YD is the total number of years (15-year for MJJAS and 14-year for NDJFM). The equation above gives a DOF of 151 and 49 for 10–20-day and 30–60-day ISOs during MJJAS, respectively. And it gives a DOF of 139 and 45 for 10–20-day and 30–60-day ISOs during NDJFM, respectively. Based on the above DOFs, we determine the correlation significant at the 95 % confidence level.

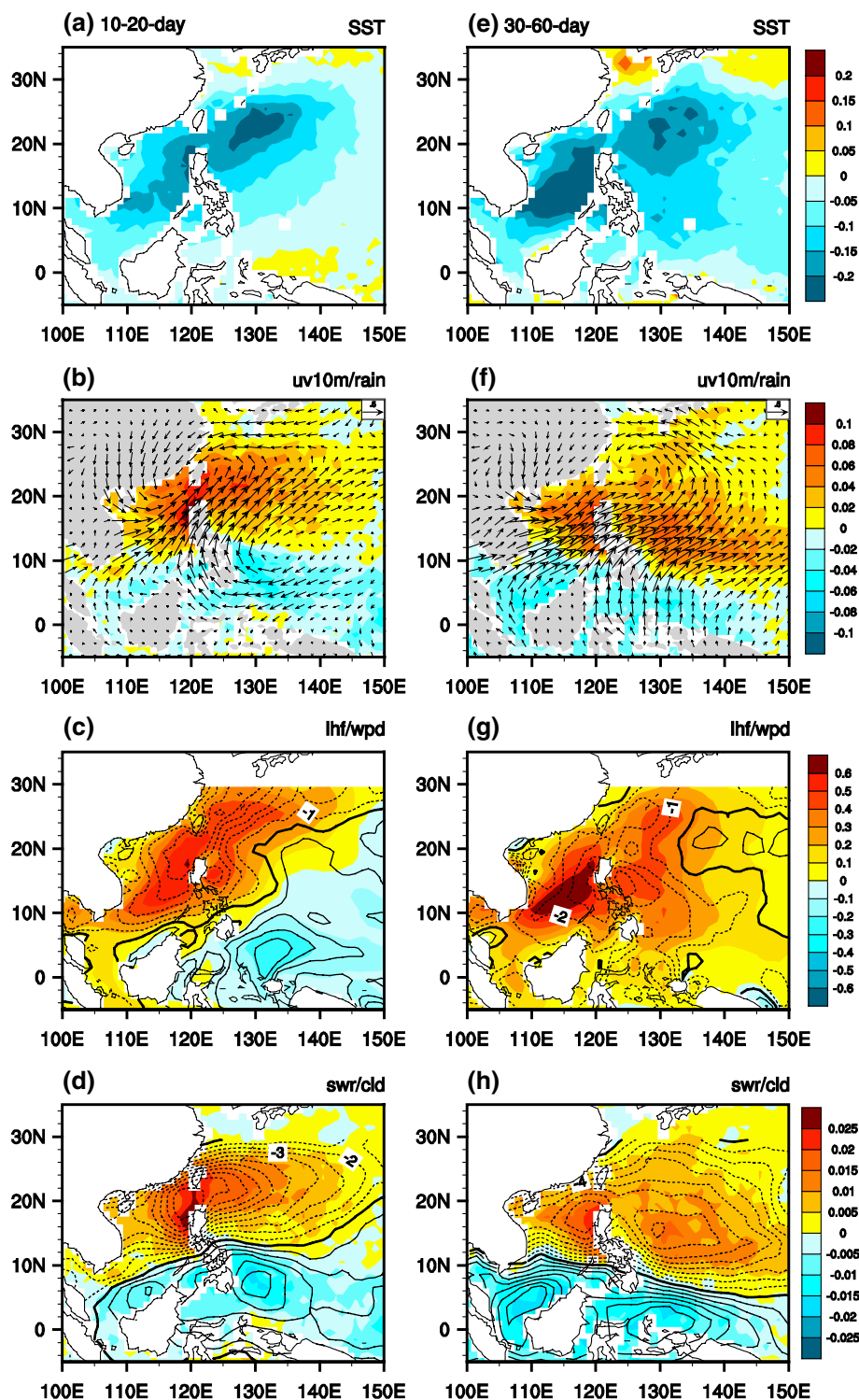
3 The dominant mode of intraseasonal SST variations

The dominant spatial patterns of 10–20-day and 30–60-day intraseasonal SST variations during summer and winter are obtained by the EOF analysis over the region of 0° – 25° N and 100° – 140° E. Note that SST anomalies in the EOF analysis are weighted to account for the decrease of area toward the pole (North et al. 1982a). In summer, the first mode of intraseasonal SST variations explains 22.9 and 34.1 % of the variance on the 10–20-day and 30–60-day time scales, respectively. In winter, the percent variance accounted for by the first mode is 25.6 and 31.9 %, respectively. In comparison, the second mode accounts for 11.5 and 15.4 % of the variance on the 10–20-day and 30–60-day time scale, respectively, during summer and 8.7 and 9.5 % of the variance on the 10–20-day and 30–60-day time scale, respectively, during winter. A lead–lag correlation analysis of the first and second PC time series shows that the first two modes are better correlated with about a quadrature phase difference in summer than in winter (figure not shown). This indicates that the propagating mode accounts for a larger part in summer than in winter.

The first modes of intraseasonal SST variations on the 10–20-day and 30–60-day time scales are well distinct from the second modes according to the method of North et al. (1982b). For brevity, the PCs on the 10–20-day and 30–60-day time scales in summer are denoted as SUM1 and SUM3, respectively, while those in winter are denoted as WIN1 and WIN3, respectively. Figures 1 and 2 show the 10–20-day and 30–60-day anomalies of SST, rain rate, 10-m zonal and meridional winds, surface wind speed, latent heat flux, cloud liquid water, and shortwave radiation in boreal summer and winter, respectively. These are obtained by regression on the respective normalized SUM1 and SUM3 or WIN1 and WIN3 time series during the period 1998–2012. The anomalies of sensible heat flux and longwave radiation are smaller than those of latent heat flux and shortwave radiation and thus they are not shown.

In MJJAS, the distribution of intraseasonal SST variations extends northeastward from the SCS to the subtropical WNP on both 10–20-day and 30–60-day time scales, with a maximum in the subtropical WNP and the SCS, respectively (Fig. 1a, e). However, the regressed anomalies of winds, rain rate, latent heat flux, shortwave radiation, and cloud liquid water display a notable difference between the 10–20-day and 30–60-day time scales. The large anomalies of the abovementioned variables extend northeastward from the SCS to the subtropical WNP on the 10–20-day time scale (Fig. 1b–d), but eastward from the SCS to the Philippine Sea on the 30–60-day time scale (Fig. 1f–h).

Fig. 1 The 10–20-day anomalies of **a** SST (*shaded*, unit: °C), **b** rain rate (*shaded*, unit: mm/day) and 10-m winds (*vector*, unit: m/s), **c** surface wind speed (*shaded*, unit: m/s) and latent heat flux (*contour*, interval: 1 W/m²), and **d** cloud liquid water (*shaded*, unit: mm) and shortwave radiation (*contour*, interval: 1 W/m²) obtained by regression on normalized SUM1 time series based on all MJJAS during the period 1998–2012. **e–h** are the same as (**a–d**) but for 30–60-day anomalies obtained by regression on normalized SUM3 time series

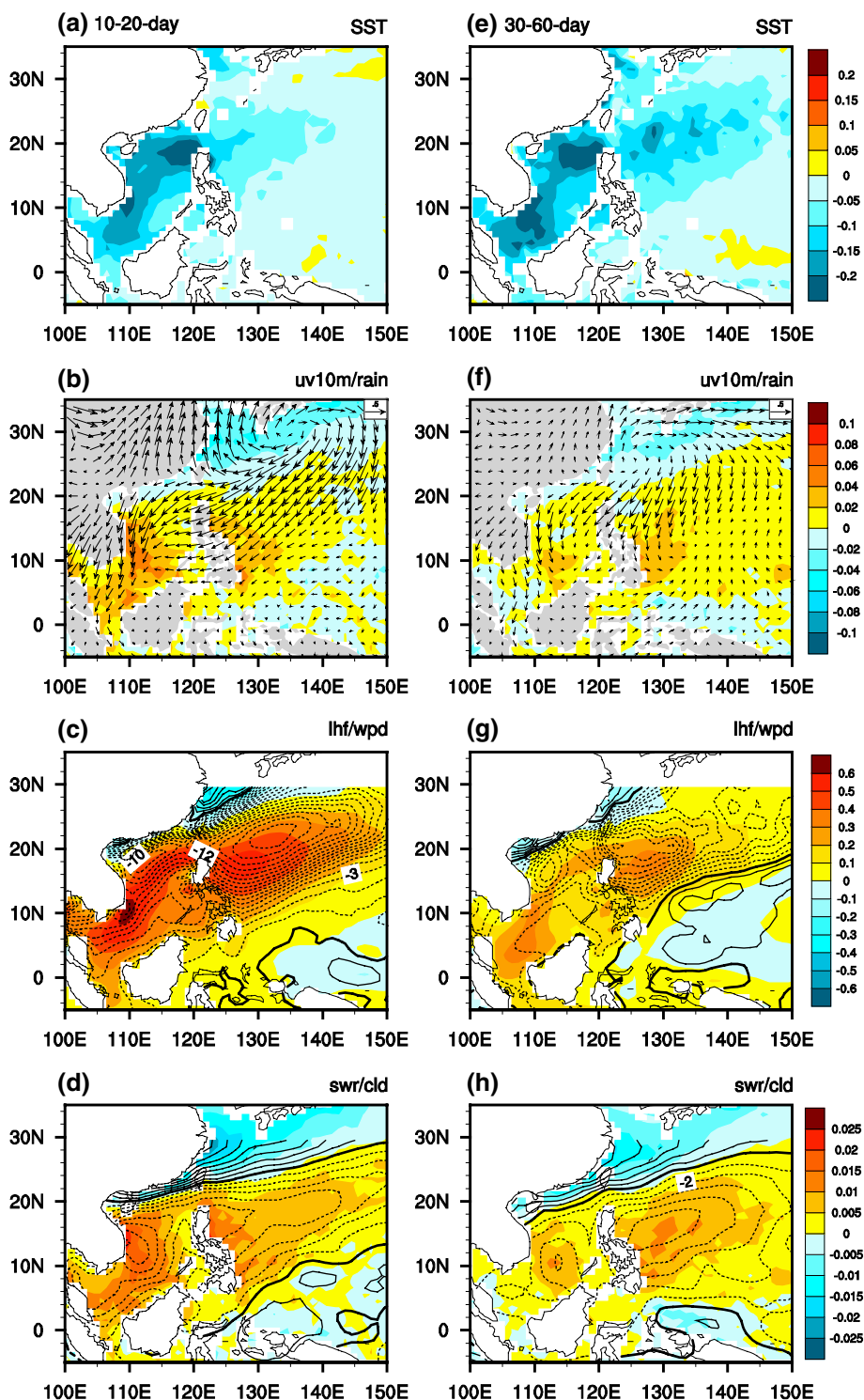


These results are generally consistent with the findings of Ye and Wu (2015).

The above differences between the 10–20-day and 30–60-day time scales may be related to the horizontal structure of wind anomalies associated with the ISOs. During summer, the wind anomalies associated with the

10–20-day ISOs feature a southwest–northeast oriented structure as shown in Fig. 1b, consistent with Mao and Chan (2005). These wind anomalies feature a Rossby-wave-like response to anomalous heating associated with more rain. Because the mean wind is southwesterly, surface wind speed is enhanced when anomalous winds are

Fig. 2 The same as Fig. 1 but for **a–d** 10–20-day anomalies obtained by regression on normalized WIN1 time series and **e–h** 30–60-day anomalies obtained by regression on normalized WIN3 time series based on all NDJFM



southwesterly (Fig. 1b). In this case, the wind speed-related upward latent heat flux anomalies are enhanced along a southwest–northeast orientation, which contributes to the SST cooling (Fig. 1a, c). Meanwhile, the southwest–northeast oriented cyclonic wind anomalies are accompanied by an increase in rain and cloud liquid water along a southwest–northeast orientation (Fig. 1b, d) and a decrease in the

shortwave radiation into the ocean (Fig. 1d), thus adding to the SST cooling (Fig. 1a). In comparison, the wind anomalies associated with the 30–60-day ISOs feature a zonal elongated structure as shown in Fig. 1f, which is consistent with Mao and Chan (2005) and Chou and Hsueh (2010). These wind anomalies feature a Rossby-wave-like response to anomalous heating as well. Under mean westerly winds,

the induced latent heat flux and shortwave radiation anomalies feature a west–east distribution, leading to a zonal extension of the high-anomaly region (Fig. 1g, h), which differs from that on the 10–20-day time scale.

While the latent heat flux and shortwave radiation anomalies are larger over the tropical than the subtropical WNP on the 30–60-day time scale (Fig. 1g, h), the corresponding SST anomalies are larger in the subtropical than the tropical WNP (Fig. 1e). This structure difference between the SST and the surface heat flux variations on the 30–60-day time scale (Fig. 1e, g, h) may be related to the mixed-layer depth change. In MJJAS, the mixed-layer depth is smaller in the subtropics than in the tropics. A tilted band with a relatively small value of <20 m lies along 20° – 30° N over the WNP [see Fig. 1b of Wu et al. (2015)]. Given a shallower mixed layer in the subtropical regions than in the tropical regions, surface heat flux is expected to be more effective in inducing SST variations in the subtropical regions. This relationship could lead to a stronger coherence of SST variation with surface heat flux variation. Thus, the SST variation in the subtropical regions between 20° and 30° N is greater than that in the tropical regions, leading to a tilted structure of SST anomalies (Fig. 1e). Note that the regressed shortwave radiation flux anomalies are larger than surface latent heat flux anomalies on both time scales. It indicates that the cloud-related shortwave radiation plays a larger role in the formation of intraseasonal SST anomalies in summer. Wu et al. (2015) showed that the latent heat flux provides a larger contribution than shortwave radiation to intraseasonal SST variations on the 10–20-day time scale. This inconsistency may be due to the different datasets of surface heat fluxes. Wu et al. (2015) used surface heat fluxes from the NCEP reanalysis and surface heat fluxes in the present study are based on the TropFlux data set.

In NDJFM, the distribution of both 10–20-day and 30–60-day intraseasonal SST variations extend northeastward from the SCS to the subtropical WNP, with the main regions in the SCS (Fig. 2a, e). This may be due to a shallower mixed layer in the SCS than in the WNP during winter [see Fig. 1a of Wu et al. (2015)]. In particular, the largest SST anomalies of about 0.2°C are observed in the northern SCS on the 10–20-day time scale (Fig. 2a) and in the northern and southwestern SCS on the 30–60-day time scale (Fig. 2e). This feature is consistent with Wu and Chen (2015) that showed there are two regions in the SCS with large 10–60-day SST standard deviation during December–February, one in the northeastern part extending westward from the Luzon Strait and the other in the southwestern part extending southward from the coast of central Vietnam. Note that the SST anomalies are relatively larger on the 30–60-day time scale than on the 10–20-day time scale.

The structure of SST anomalies is associated with the wind perturbation. During winter, the northerly or

northeasterly wind perturbations feature a southwest–northeast distribution over the SCS and WNP (Fig. 2b, f), which is consistent with Wu and Chen (2015). Under mean northeasterly winds, large latent heat flux and shortwave radiation anomalies tend to be oriented along a southwest–northeast direction (Fig. 2c, d, g, h), leading to a similar distribution of SST anomalies. In addition, the regressed latent heat flux anomalies are larger than shortwave radiation anomalies on both the 10–20-day and 30–60-day time-scales. This is different from that in MJJAS (Fig. 2c, d, g, h). This appears to relate to the fact that the convective rain is weak over the Northern Hemisphere in boreal winter. Note that less rain is overlaid by anticyclonic divergent wind anomalies and more rain is overlaid by cyclonic convergent wind anomalies over the SCS and WNP (Fig. 2b, f). This indicates a role of atmospheric circulation in inducing rain anomalies in winter.

The spatial phase relationship between SST and latent heat flux anomalies and between SST and shortwave radiation anomalies (Figs. 1, 2) shows a large difference between summer and winter. In MJJAS, negative surface heat flux anomalies are located to north side of negative SST anomalies, whereas in NDJFM, negative surface heat flux anomalies are located to the south side of negative SST anomalies. This difference in phase relationship indicates a different direction of propagation of SST anomalies between summer and winter. This will be discussed in detail in the next section.

4 Propagation of intraseasonal SST anomalies and contribution of surface heat flux

To understand the propagation of SST anomalies, we examine the spatial–temporal evolution of intraseasonal SST anomalies and associated surface heat flux anomalies. The normalized SUM1/SUM3 and WIN1/WIN3 are regarded as a reference to construct the evolving anomalies through the lag–lead regression for summer and winter, respectively. For example, in Figs. 3 and 7, the anomalies are shown starting from 6 days before (lead -6) to 6 days after (lag $+6$) the SUM1 and WIN1 on the 10–20-day time scale, while on the 30–60-day time scale they start from 16 days before (lead -16) to 16 days after (lag $+16$) the SUM3 and WIN3. Note that only the anomalies with the corresponding correlations significant at the 95 % confidence level are shown. We will analyze the relationship in summer first, and then that in winter.

4.1 Boreal summer

In MJJAS, southwest–northeast tilted SST anomalies propagate northwestward on the 10–20-day time scale in

Fig. 3 a–e The 10–20-day SST anomalies (unit: °C) from 6 days before (lead – 6) to 6 days after (lag + 6) obtained by regression on normalized SUM1 time series based on all MJJAS during the period 1998–2012. f–j The same as Fig. 3a–e, but for the 30–60-day SST anomalies from 16 days before (lead – 16) to 16 days after (lag + 16) obtained by regression on normalized SUM3 time series. The red dashed lines denote the cross section, which will be used in Fig. 5. Only the anomalies with the corresponding correlations significant at the 95 % confidence level are shown

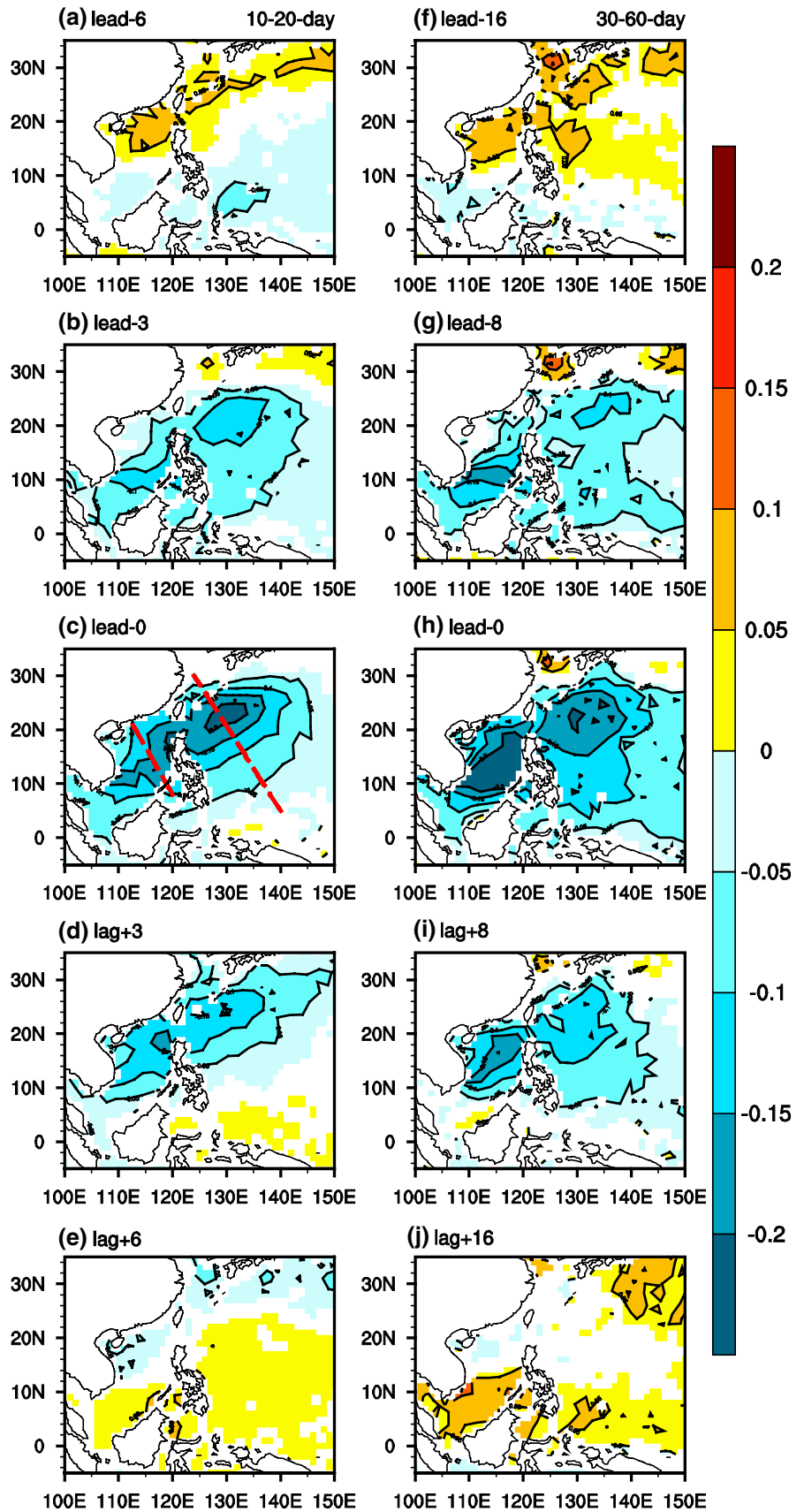
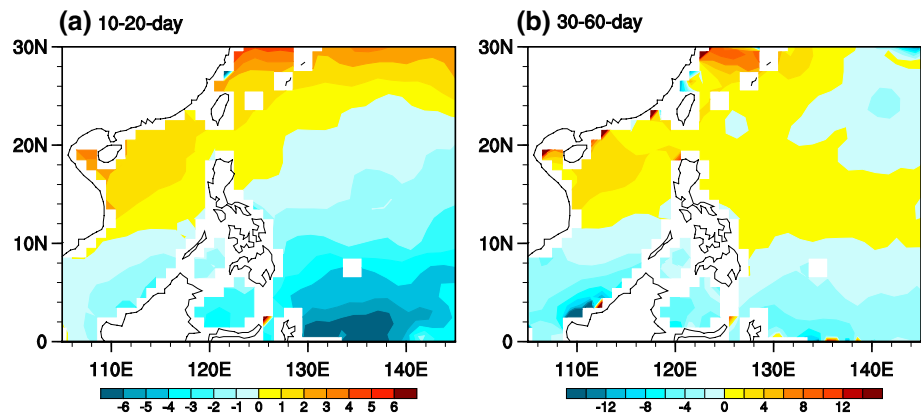


Fig. 4 The corresponding days of minimum SST anomalies leading/lagging a SUM1 on the 10–20-day time scale and b SUM3 on the 30–60-day time scale. The direction of time increase indicates the direction of propagation of SST anomalies



the SCS and the WNP (Fig. 3a–e). At lead-6 day, negative SST anomalies appear in the southern SCS and the tropical WNP (Fig. 3a). At lead-3 day, a southwest–northeast tilted band of negative SST anomalies develop in the central part of the SCS and the subtropical WNP (Fig. 3b). Three days later, the negative SST anomalies intensify and move northwestward (Fig. 3c). At lag + 3 day, the negative SST anomalies weaken in the SCS and the WNP and continue to move northwestward and positive SST anomalies develop in the equatorial western Pacific (Fig. 3d). At lag + 6 day, the negative SST anomalies are gradually replaced by the positive anomalies in the southern SCS and tropical WNP (Fig. 3e). On the 30–60-day time scale, the SST anomalies display obvious northward propagation over the SCS. Negative SST anomalies appear in the southern SCS (Fig. 3f), intensify and move northward (Fig. 3g, h), weaken (Fig. 3i, j). The propagation is not clear in the WNP except for the low latitude region (Fig. 3f, j).

In order to illustrate more clearly the direction of propagation of SST anomalies, we extract the days corresponding to minimum SST anomalies based on a lead–lag regression and plot them in one figure. First, we calculate the SST anomalies at each grid point regressed with respect to the normalized SUM1 on the 10–20-day time scale within the time window of -10 to 10 day and with respect to the normalized SUM3 on the 30–60-day time scale within the time window of -30 to 30 day, respectively. Then, the time corresponding to the minimum value is determined at each grid point based on the temporal evolution of the SST anomalies. The results are displayed in Fig. 4a for the 10–20-day time scale and in Fig. 4b for the 30–60-day time scale. The direction of time increase indicates the direction of propagation of SST anomalies. On the 10–20-day time scale, the days of minimum SST anomalies are tilted along a southwest–northeast band and increase northwestward in the SCS and the WNP (Fig. 4a). This indicates a northwestward propagation of 10–20-day SST anomalies. On the 30–60-day time scale, the days of minimum SST anomalies

display a west–east distribution in the SCS and the tropical WNP (Fig. 4b). This denotes a northward propagation of 30–60-day SST anomalies.

To further understand the propagation of SST anomalies and the relationship between SST and surface heat flux variations, we display Hovmöller diagrams of anomalies of different variables. For the 10–20-day time scale, we select two southeast–northwest cross sections as shown in Fig. 3c. The results are displayed in Fig. 5. For the 30–60-day time scale, we show two cross-sections, one along 105° – 120° E and the other along 120° – 140° E. The former represents the SCS region and the latter represents the WNP region. The results are displayed in Fig. 6.

On the 10–20-day time scale, the SST anomalies take about 4 days to move from the southeastern SCS to the coast of South China (Fig. 5a, b). It takes about 8 days for the SST anomalies to move from the equatorial western Pacific to the coast of eastern China (Fig. 5c, d). The maximum SST anomalies are located south of 15° N in the SCS (Fig. 5a, b), while they occur near 24° N in the WNP (Fig. 5c, d). The surface latent heat flux and shortwave radiation anomalies also display a northwestward propagation from the equatorial region to the subtropics. Meanwhile, both negative surface latent heat flux and shortwave radiation anomalies lead negative SST anomalies in both the SCS and the WNP regions by about 4 days. The magnitude of shortwave radiation anomalies are larger than that of latent heat flux anomalies at the low latitudes, but the two are comparable in the subtropics (Fig. 5). This indicates that the cloud–radiation effect is a more important factor for the SST propagation, and the wind–evaporation effect is supplementary on the 10–20-day time scale over the SCS and WNP regions.

On the 30–60-day time scale, the SST anomalies in the SCS show an obvious northward propagation (Fig. 6a, b). The northward propagation feature is observed only south of 18° N in the WNP (Fig. 6c, d). Both negative latent heat flux and shortwave radiation

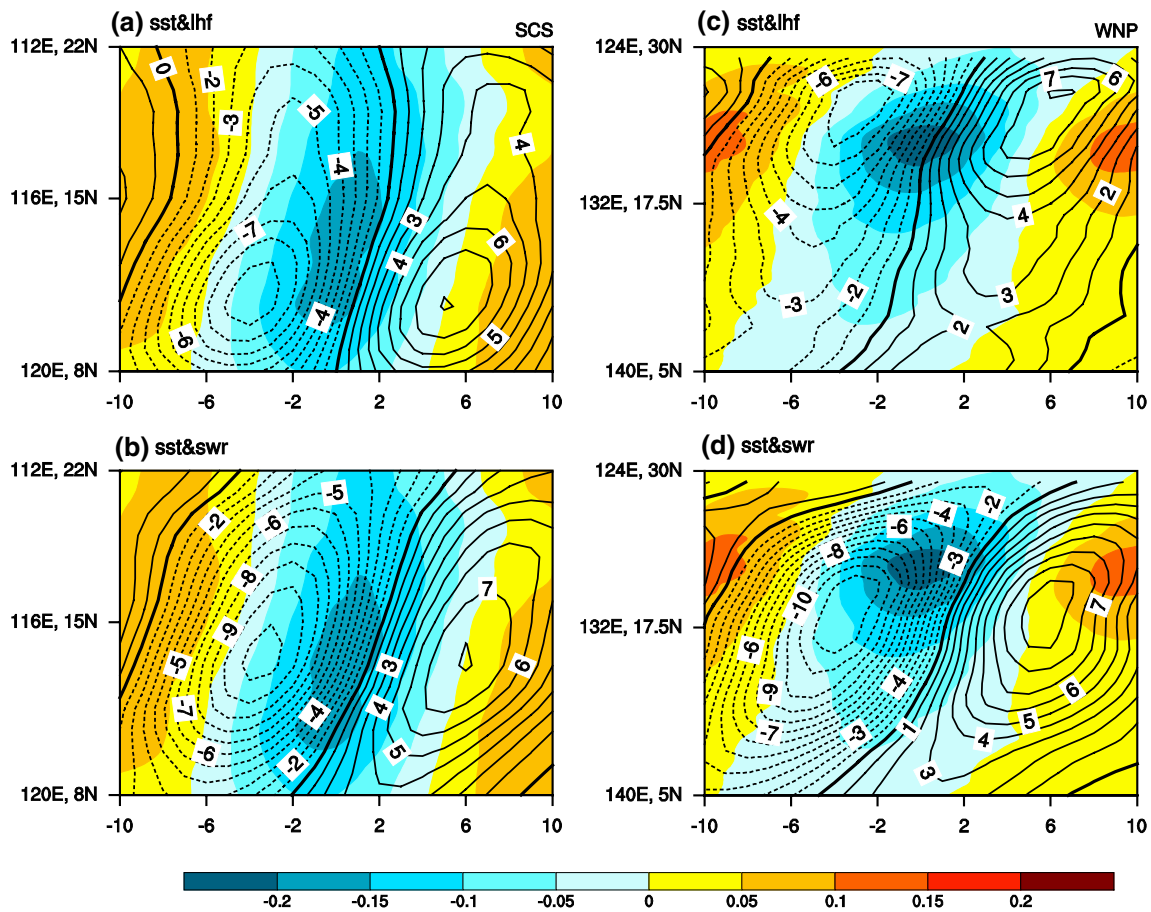


Fig. 5 Hovmöller diagrams of 10–20-day **a** SST (*shaded*, unit: °C) and latent heat flux anomalies (*contour*, interval: 1 W/m²) and **b** SST (*shaded*, unit: °C) and shortwave radiation anomalies (*contour*, interval: 1 W/m²) along the *dashed line* over the SCS in Fig. 3c from

10 days before to 10 days after the SUM1 time series obtained by regression with respect to the normalized SUM1 time series based on all MJJAS during the period 1998–2012. **c, d** The same as Fig. 5a, b, but along the *dashed line* over the WNP in Fig. 3c

anomalies lead negative SST anomalies in the SCS and the WNP by about 10 days. Meanwhile, shortwave radiation anomalies display an obvious northward propagation in both the SCS and the WNP regions (Fig. 6b, d). However, surface latent heat flux anomalies tend to be simultaneous over the SCS (Fig. 6a). This indicates that the cloud–radiation effect is an important factor for the northward propagation of SST anomalies in the SCS. In comparison, over the WNP, surface latent heat flux anomalies tend to appear earlier over the subtropics (Fig. 6c). South of 20°N over the WNP, the magnitude of shortwave radiation anomalies is two times greater than that of surface latent heat flux anomalies (Fig. 6c, d). This indicates that the shortwave radiation plays a larger role in the SST propagation compared to surface latent heat flux. North of 20°N over the WNP, the time lag between SST and shortwave radiation anomalies is small. This indicates that surface latent heat flux or other oceanic processes may be responsible for the SST changes.

4.2 Boreal winter

In NDJFM, the intraseasonal SST anomalies display southward propagation on both the 10–20-day and 30–60-day time scales, which is opposite to that in MJJAS. On the 10–20-day time scale, at lead-6 day, the SST anomalies are positive over the SCS and most of the WNP (Fig. 7a). At lead-3 day, a center of negative SST anomaly appears in the northeastern part of the SCS (Fig. 7b). Three days later, the negative SST anomalies intensify and move southward (Fig. 7c). At lag + 3 day, the negative SST anomalies weaken in the SCS with the largest anomalies near the coast of central Vietnam (Fig. 7d). Positive SST anomalies appear at lag + 6 day (Fig. 7e), with the largest anomalies in the northern SCS. On the 30–60-day time scale, the SST anomalies display changes similar to those on the 10–20-day time scale, but with relatively larger anomalies (Fig. 7f–j) compared to the 10–20-day time scale.

The propagation of SST anomalies is more clearly depicted by the spatial change in the time of minimum

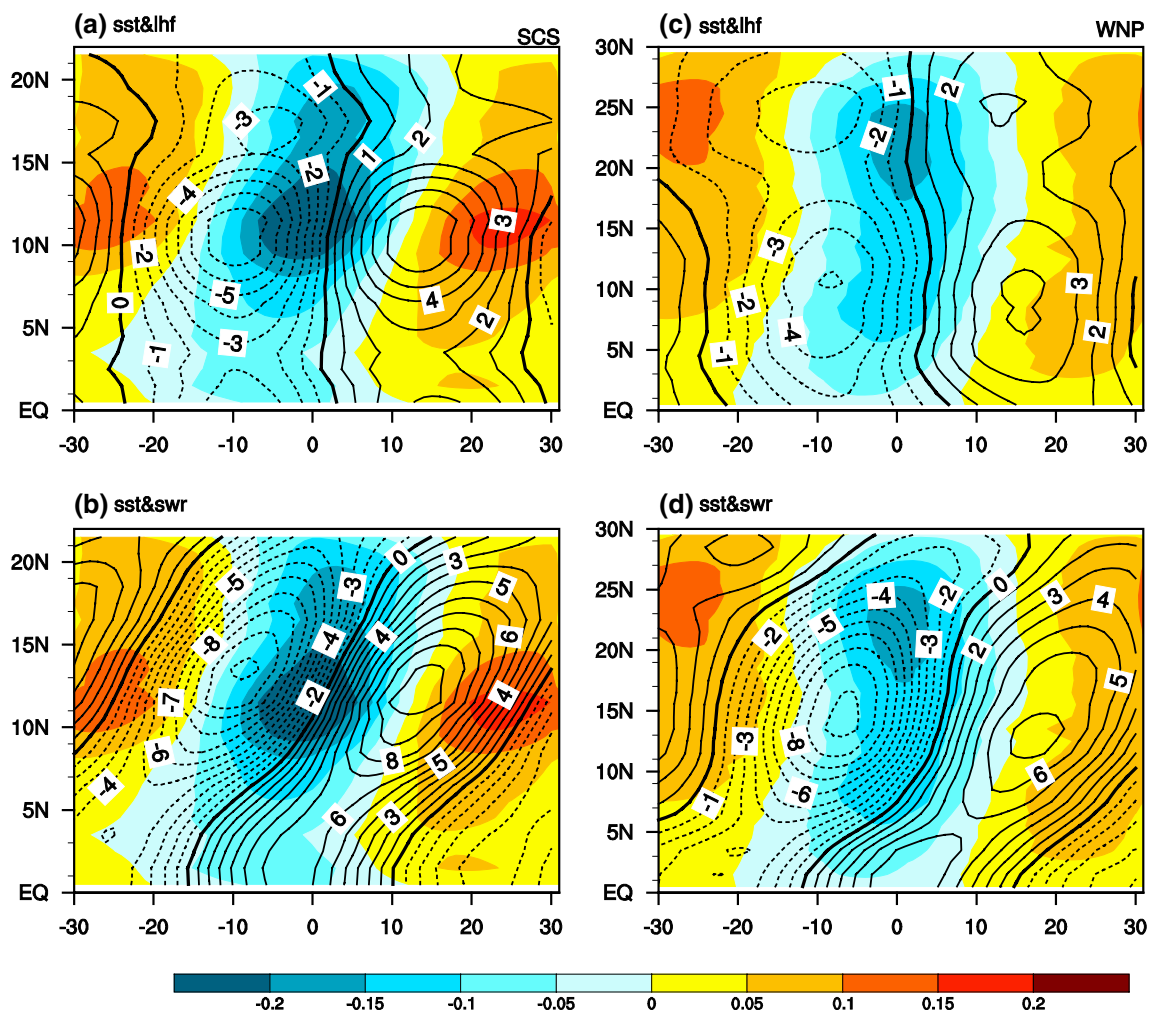


Fig. 6 The same as Fig. 5 but for the 30–60-day anomalies averaged between **a, b** 105°E and 120°E and between **c, d** 120°E and 140°E from 30 days before to 30 days after the SUM3 time series obtained

by regression with respect to the normalized SUM3 time series based on all MJJAS during the period 1998–2012, respectively

SST anomalies with respect to the WIN1 on the 10–20-day time scale and WIN3 on the 30–60-day time scale shown in Fig. 8a, b, respectively. The time for the appearance of minimum SST anomalies shows a southward increase in the SCS on both time scales (Fig. 8). In the subtropical WNP, the southward increase is also observed on the 10–20-day time scale (Fig. 8a). This supports the southward propagation of both 10–20-day and 30–60-day SST anomalies in the SCS and the 10–20-day SST anomalies in the subtropical WNP. The time of minimum SST anomalies shows a northward increase in the tropical WNP on the 10–20-day time scale (Fig. 8a) and in the WNP on the 30–60-day time scale (Fig. 8b).

Similar to those in MJJAS, the Hovmöller diagrams of anomalies of different variables along 105°–120°E and 120°–140°E are shown in Figs. 9 and 10 on the two time scales for further illustration of the propagation feature. On

the 10–20-day time scale, the SST anomalies take about 2 days to move from the coast of South China to the equatorial region over the SCS (Fig. 9a, b). The maximum of SST anomalies is located in the northern SCS. The latent heat flux anomalies display an obvious southward propagation over the whole SCS (Fig. 9a), while the shortwave radiation anomalies show a southward propagation only in the subtropics over the SCS (Fig. 9b). In the main region of SST propagation, surface latent heat flux anomalies are much larger than shortwave radiation anomalies over the SCS (Fig. 9a, b). This strongly indicates that the wind–evaporation effect is more important than the cloud–radiation effect for the southward propagation of SST anomalies. In comparison, the SST anomalies over the WNP are much weaker than those over the SCS with the maximum near 20°N, and southward propagation of SST anomalies is not clear (Fig. 9c, d). Surface latent heat flux and shortwave

Fig. 7 The same as Fig. 3 but for **a–e** 10–20-day SST anomalies obtained by regression on normalized WIN1 time series and **f–j** 30–60-day SST anomalies obtained by regression on normalized WIN3 time series based on all NDJFM

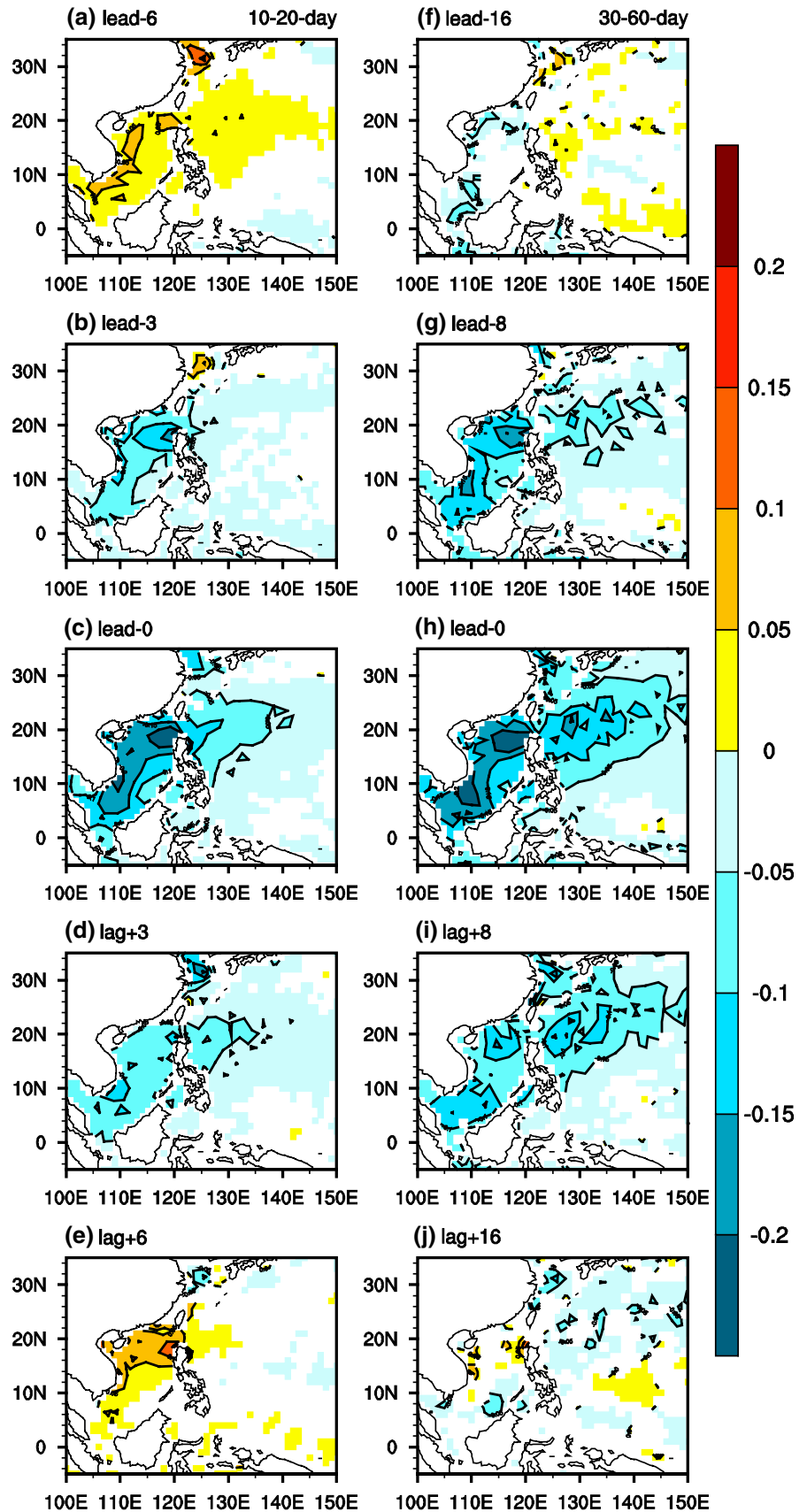


Fig. 8 The corresponding days of minimum SST anomalies leading/lagging **a** WIN1 on the 10–20-day time scale and **b** WIN3 on the 30–60-day time scale. The direction of time increase indicates the direction of propagation of SST anomalies

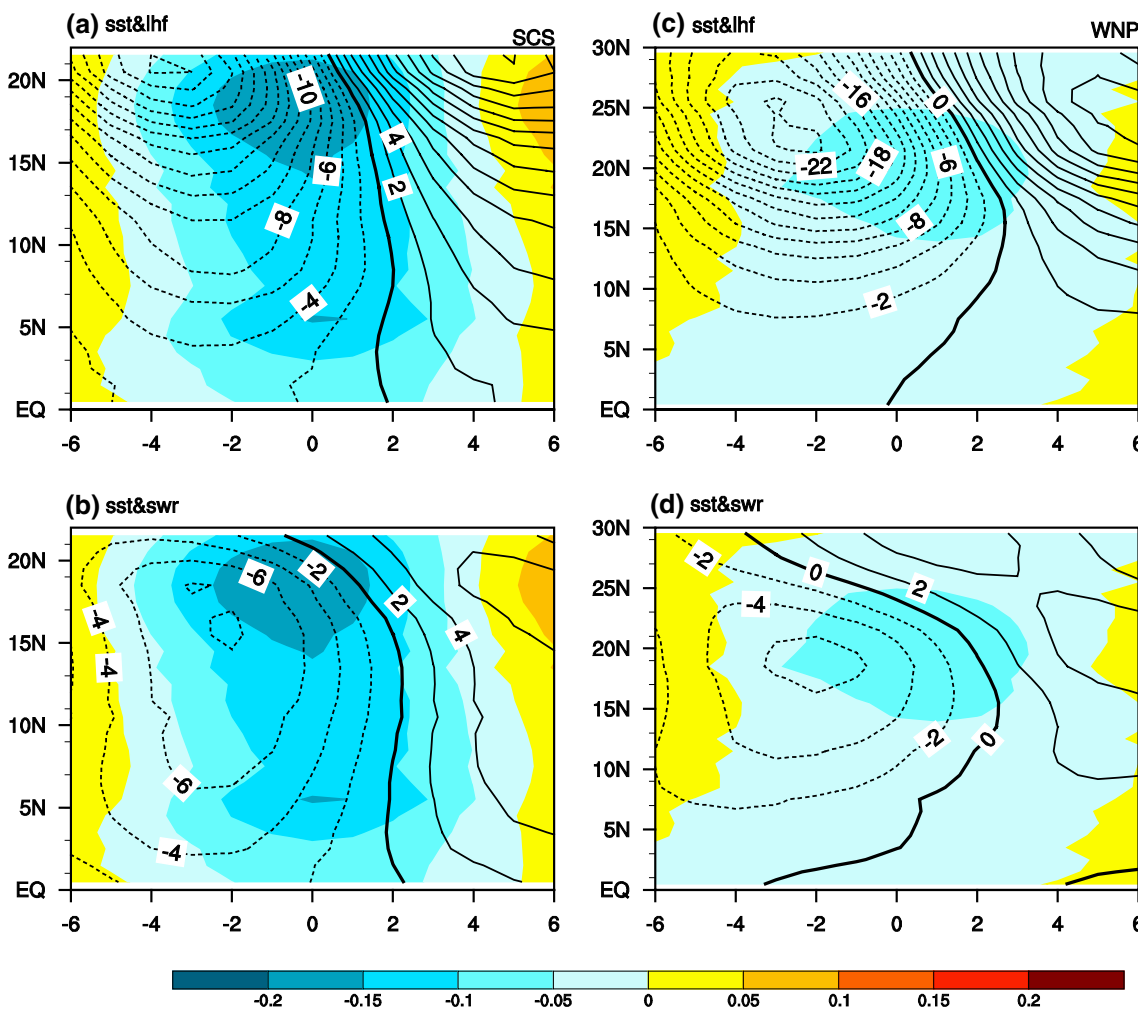
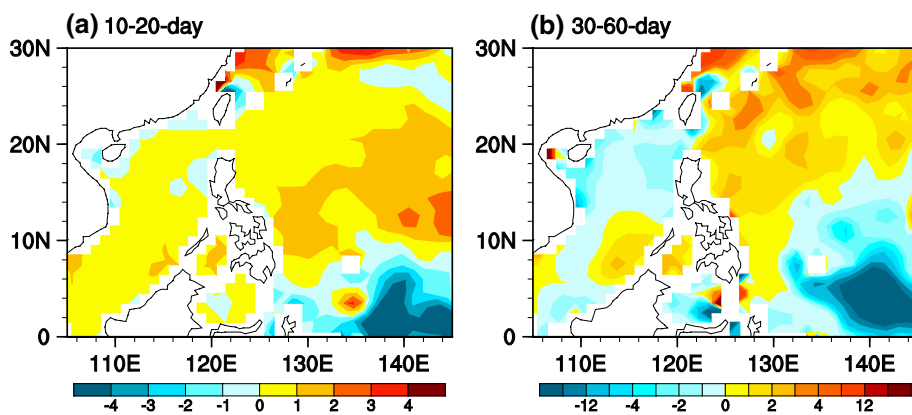


Fig. 9 The same as Fig. 5 but for the anomalies averaged between **a**, **b** 105°E and 120°E and between **c**, **d** 120°E and 140°E from 6 days before to 6 days after the WIN1 time series obtained by regression

with respect to the normalized WIN1 time series based on all NDJFM during the period 1998–2012

radiation anomalies display an obvious southward propagation north of 15°N, with a larger magnitude in the former than in the latter. It indicates that other oceanic processes may be important for the SST change in the WNP.

On the 30–60-day time scale, the propagation of SST anomalies and associated surface heat flux anomalies displays features similar to those on the 10–20-day time scale (Figs. 9, 10). The magnitude of the SST anomalies

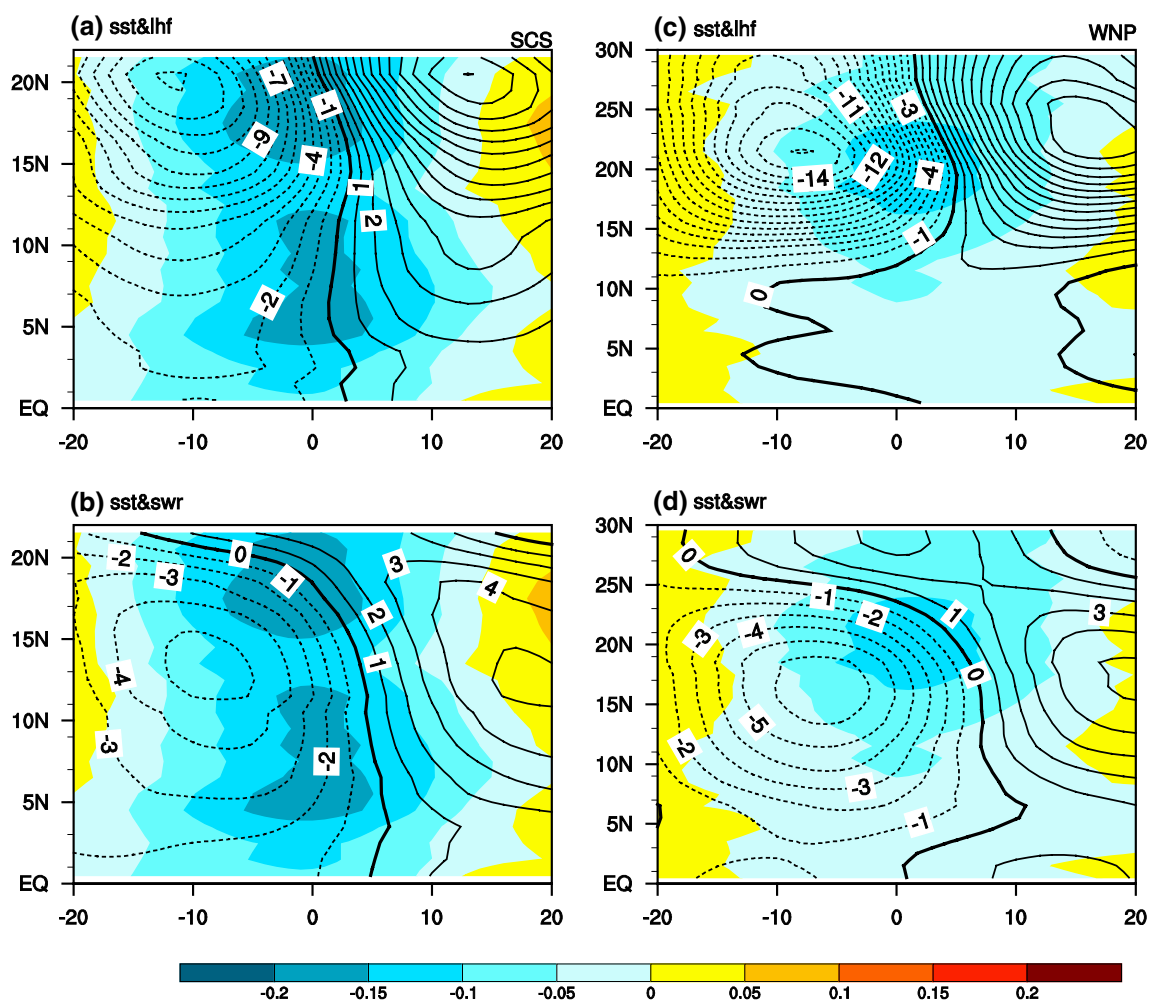


Fig. 10 The same as Fig. 6 but for the anomalies from 20 days before to 20 days after the WIN3 time series obtained by regression with respect to the normalized WIN3 time series based on all NDJFM during the period 1998–2012

in the SCS and the WNP are relatively larger than that on the 10–20-day time scale. In addition, two centers of SST anomalies are observed over the northern and southern SCS (Fig. 10a, b). In comparison, the magnitude of surface latent heat flux anomalies is larger than that of shortwave radiation anomalies. The above features indicate that surface latent heat flux plays a leading role in the southward propagation of SST anomalies over the whole SCS on the 30–60-day time scale. The southward propagation of SST anomalies is not clear in the WNP (Fig. 10c, d). Furthermore, the relationship between SST and latent heat flux is more coherent over the SCS than over the WNP, which may be due to the relatively small mixed-layer depth in the SCS.

5 Summary and discussions

The present study contrasts the structure and propagation of intraseasonal SST perturbations and effects of surface

heat flux variations on the 10–20-day and 30–60-day time scales during boreal summer and winter in the SCS and the WNP regions. Notable differences have been detected in the propagation of intraseasonal SST perturbations and relative contributions of surface latent heat flux and shortwave radiation to the SST propagation between summer and winter.

In summer, the spatial distributions of the leading SST modes on the 10–20-day and 30–60-day time scales feature a tilted southwest–northeast band from the SCS to the subtropical WNP, but with a larger value in the subtropical WNP on the 10–20-day time scale and in the SCS on the 30–60-day time scale. However, there is a clear difference in the distribution of the associated anomalies of surface heat flux, surface wind speed, and cloud liquid water between the 10–20-day and 30–60-day time scales. The large anomalies are observed along a tilted southwest–northeast band from the SCS to the subtropics on the 10–20-day time scale and along a zonal elongated band

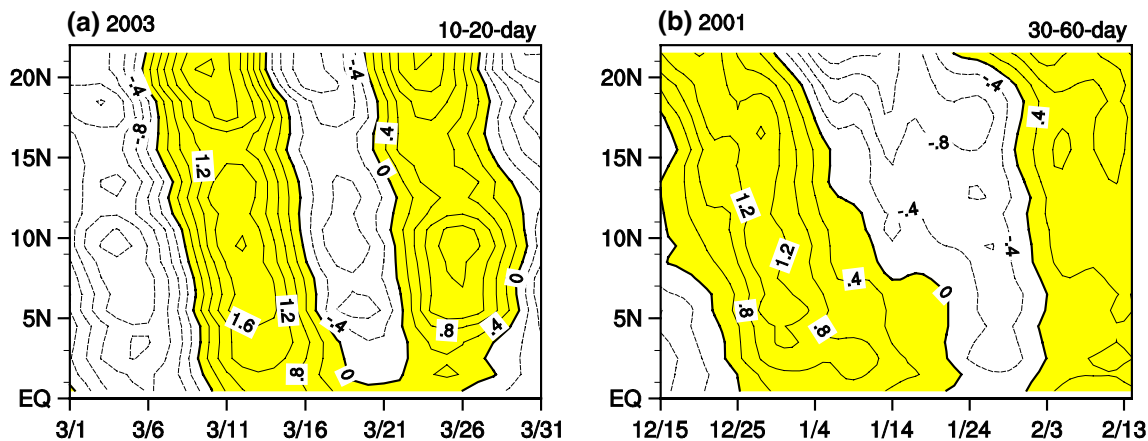


Fig. 11 **a** Hovmöller diagrams of wind speed anomalies (contour, interval: 0.4 m/s) at 10 m on the 10–20-day time scale along 105°–120°E during March 1 through March 31 of 2003. **b** The same

as Fig. 11a but on the 30–60-day time scale during December 15 of 2000 through February 13 of 2001. The *shadings* denote that the value is more than zero

over the SCS and the Philippine Sea on the 30–60-day time scale. This difference is mainly associated with the horizontal structure of the wind anomalies associated with the ISOs. During summer, the wind anomalies associated with the ISOs display a southwest–northeast oriented structure on the 10–20-day time scale, but a zonal elongated structure on the 30–60-day time scale (Mao and Chan 2005). This indicates the importance of the structure of atmospheric ISOs in determining the distribution of large surface heat flux variations. In addition, the inconsistency between horizontal structures of SST and the atmospheric variables on the 30–60-day time scale may be associated with the mixed-layer depth change.

In winter, the dominant spatial structures of 10–20-day and 30–60-day intraseasonal SST variations both extend northeastward from the SCS to the subtropical WNP, with the maximums in the SCS. This is due to the shallower mixed layer in the SCS than in the WNP. A similar spatial structure is observed in surface wind and surface heat flux anomalies on both the 10–20-day and 30–60-day time scales.

In summer, the SST anomalies show obvious northwestward and northward propagations, respectively, on the 10–20-day and 30–60-day time scales in the SCS. The northwestward propagation is also obvious in the WNP on the 10–20-day time scale, while it is mainly confined to south of 20°N in the WNP. The shortwave radiation contribution to the SST propagation appears to be more important on the 30–60-day time scale over the SCS–WNP region, while the shortwave radiation contribution is comparable to the latent heat flux contribution on the 10–20-day time scale in the SCS–WNP region. This indicates that the cloud–radiation effect is an important factor for the SST propagation on both 10–20-day and 30–60-day time scales

in the SCS and the WNP, and wind–evaporation effect is supplementary on the 10–20-day time scale.

In winter, the SST anomalies show southward propagation on the 10–20-day and 30–60-day time scales in the whole SCS, while the southward propagation feature of SST anomalies is weak and not obvious in the WNP. The latent heat flux anomalies show a larger contribution to the SST propagation compared to shortwave radiation anomalies on both time scales in the SCS. This indicates that the latent heat flux is a leading factor in the southward propagation of intraseasonal SST signals in the SCS. Although the SST anomalies are weak in the WNP on both time scales, the latent heat flux and shortwave radiation anomalies show an obvious southward propagation in the subtropical WNP, with the larger magnitude in the former than in the latter. Meanwhile, the SST and latent heat flux variations have a higher coherence in the SCS than in the WNP on both time scales due to the relatively small mixed-layer depth in winter.

The northward propagation of the intraseasonal variations of SST and associated atmospheric winds in the SCS and the WNP has been shown by previous studies. In this study and Wu (2016), the southward propagations in intraseasonal SST and surface latent heat flux and shortwave radiation variations in winter have been illustrated through the observational data. Figure 11 further displays Hovmöller diagrams of 10-m wind speed anomalies along 105°–120°E on the 10–20-day and 30–60-day time scales during winter in two selected cases. Obvious southward propagation is observed from the coast of South China to the equatorial region in both cases. Examination of other times in winter reveals that northward propagation of wind speed anomalies also occurs over the SCS. Previous studies have shown that the northward propagation of

atmospheric ISOs in summer is associated with the vertical shear, moisture–convection feedback, and vorticity advection mechanisms (Jiang et al. 2004; Chou and Hsueh 2010). The southward propagation of atmospheric ISOs in winter, however, is not yet examined. The southward propagation of atmospheric ISOs in winter may imply that some different mechanisms could be at work over the SCS region. What are the specific mechanisms for such southward propagation of atmospheric ISOs remains to be investigated. The coherence in the southward propagation of SST and surface wind perturbations identified by Wu (2016) and this study appears to suggest a role of air–sea coupling. In the future, efforts will be made to contrast the mechanisms of northward and southward propagations of atmospheric ISOs over the SCS in winter.

Acknowledgments This study is supported by National Natural Science Foundation of China (Grant Nos. 41475081, 41275081, 41505048, and 41530425) and the LASW State Key Laboratory Special Fund (Grant No. 2015LASW-B04). The TMI data were obtained from <http://www.remss.com/missions/tmi>. The TropFlux data were obtained from <http://www.incois.gov.in/tropflux/overview.html>. The NCEP reanalysis 2 data were obtained from <ftp://ftp.cdc.noaa.gov/>.

References

- Annamalai H, Slingo JM (2001) Active/break cycles: diagnosis of the intraseasonal variability of the Asian summer monsoon. *Clim Dyn* 18:85–102
- Chou C, Hsueh YC (2010) Mechanisms of northward-propagating intraseasonal oscillation—a comparison between the Indian Ocean and the western North Pacific. *J Clim* 23:6624–6640
- Duvel JP, Vialard J (2007) Indo-Pacific sea surface temperature perturbations associated with intraseasonal oscillations of tropical convection. *J Clim* 20:3056–3082
- Fu X, Wang B, Li T, McCreary JP (2003) Coupling between northward propagating, intraseasonal oscillations and sea-surface temperature in the Indian Ocean. *J Atmos Sci* 60:1733–1753
- Fukutomi Y, Yasunari T (1999) 10–25-Day intraseasonal variations of convection and circulation over East Asia and western North Pacific during early summer. *J Meteorol Soc Japan* 77:753–769
- Gao RZ, Zhou FX (2002) Monsoonal characteristics revealed by intraseasonal variability of sea surface temperature (SST) in the South China Sea (SCS). *Geophys Res Lett* 29:1222. doi:10.1029/2001GL014225
- Hsu HH (1996) Global view of the intraseasonal oscillation during northern winter. *J Clim* 9:2386–2406
- Hsu HH, Weng CH (2001) Northwestward propagation of the intraseasonal oscillation in the western North Pacific during the boreal summer: structure and mechanism. *J Clim* 14:3834–3850
- Hsu HH, Weng CH, Wu CH (2004) Contrasting characteristics between the northward and eastward propagation of the intraseasonal oscillation during the boreal summer. *J Clim* 17:727–743
- Jiang X, Li T, Wang B (2004) Structures and mechanisms of the northward-propagating boreal summer intraseasonal oscillation. *J Clim* 17:1022–1039
- Kajikawa Y, Yasunari T (2005) Interannual variability of the 10–25- and 30–60-day variation over the South China Sea during boreal summer. *Geophys Res Lett* 32:L04710. doi:10.1029/2004GL021836
- Kanamitsu M, Ebisuzaki W, Woollen J, Yang SK, Hnilo JJ, Fiorino M, Potter GL (2002) NCEP–DOE AMIP-II reanalysis (R-2). *Bull Am Meteorol Soc* 83:1631–1643
- Kemball-Cook S, Wang B (2001) Equatorial waves and air–sea interaction in the boreal summer intraseasonal oscillation. *J Clim* 14:2923–2942
- Kikuchi K, Wang B (2009) Global perspective of the quasi-biweekly oscillation. *J Clim* 22:1340–1359
- Kumar BP, Vialard J, Lengaigne M, Murty VSN, McPhaden MJ (2012) TropFlux: air–sea fluxes for the global tropical oceans—description and evaluation. *Clim Dyn* 38:1521–1543. doi:10.1007/s00382-011-1115-0
- Lau KM, Sui CH (1997) Mechanisms of short-term sea surface temperature regulation: observations during TOGA COARE. *J Clim* 10:465–472
- Madden RA, Julian PR (1971) Detection of a 40–50 day oscillation in the zonal wind in the tropical Pacific. *J Atmos Sci* 28:702–708
- Madden RA, Julian PR (1972) Description of global-scale circulation cells in the tropics with a 40–50 day period. *J Atmos Sci* 29:3138–3158
- Maloney ED, Sobel AH (2004) Surface fluxes and ocean coupling in the tropical intraseasonal oscillation. *J Clim* 17:4368–4386
- Mao JY, Chan JCL (2005) Intraseasonal variability of the South China Sea summer monsoon. *J Clim* 18:2388–2402
- North GR, Moeng FJ, Bell TL, Cahalan RF (1982a) The latitude dependence of the variance of zonally averaged quantities. *Mon Weather Rev* 110:319–326
- North GR, Bell TL, Cahalan RF, Moeng FJ (1982b) Sampling errors in the estimation of empirical orthogonal functions. *Mon Weather Rev* 110:699–706
- Roxy M, Tanimoto Y (2012) Influence of sea surface temperature on the intraseasonal variability of the South China Sea summer monsoon. *Clim Dyn* 39:1209–1218
- Sengupta D, Goswami B, Senan R (2001) Coherent intraseasonal oscillations of ocean and atmosphere during the Asian summer monsoon. *Geophys Res Lett* 28:4127–4130
- Vecchi GA, Harrison DE (2002) Monsoon breaks and subseasonal sea surface temperature variability in the Bay of Bengal. *J Clim* 15(12):1485–1493
- Wang B, Rui H (1990) Synoptic climatology of transient tropical intraseasonal convection anomalies: 1975–1985. *Meteorol Atmos Phys* 44:43–61
- Wang B, Wu R (1997) Peculiar temporal structure of the South China Sea summer monsoon. *Adv Atmos Sci* 14:177–194
- Wentz FJ, Gentemann C, Smith D, Chelton D (2000) Satellite measurements of sea surface temperature through clouds. *Science* 288:847–850
- Wheeler M, Kiladis GN (1999) Convectively coupled equatorial waves: analysis of clouds and temperature in the wavenumber-frequency domain. *J Atmos Sci* 56:374–399
- Woolnough SJ, Slingo JM, Hoskins BJ (2000) The relationship between convection and sea surface temperature on intraseasonal timescales. *J Clim* 13:2086–2104
- Wu R (2010) Subseasonal variability during the South China Sea summer monsoon onset. *Clim Dyn* 34:629–642. doi:10.1007/s00382-009-0679-4
- Wu R (2016) Coupled intraseasonal variations in the East Asian winter monsoon and the South China Sea–western North Pacific SST in boreal winter. *Clim Dyn*. doi:10.1007/s00382-015-2949-7
- Wu R, Chen Z (2015) Intraseasonal SST variations in the South China Sea during boreal winter and impacts of the East Asian winter monsoon. *J Geophys Res* 120:5863–5878. doi:10.1002/2015JD023368
- Wu R, Kirtman BP, Pegion K (2008) Local rainfall–SST relationship on subseasonal time scales in satellite observations and CFS. *Geophys Res Lett* 35:L22706. doi:10.1029/2008GL035883

- Wu R, Cao X, Chen SF (2015) Co-variations of SST and surface heat flux on 10–20-day and 30–60-day time scales over the South China Sea and western North Pacific. *J Geophys Res* 120:12486–12499. doi:[10.1002/2015JD024199](https://doi.org/10.1002/2015JD024199)
- Xie SP, Chang CH, Xie Q, Wang D (2007) Intraseasonal variability in the summer South China Sea: wind jet, cold filament, and recirculations. *J Geophys Res* 112(C10):C10008. doi:[10.1029/2007jc004238](https://doi.org/10.1029/2007jc004238)
- Yasunari T (1981) Structure of an Indian summer monsoon system with around 40-day period. *J Meteorol Soc Japan* 59:336–354
- Ye KH, Wu R (2015) Contrast of local air-sea relationship between 10–20-day and 30–60-day intraseasonal oscillations during May–September over the South China Sea and the western North Pacific. *Clim Dyn* 45:3441–3459. doi:[10.1007/s00382-015-2549-6](https://doi.org/10.1007/s00382-015-2549-6)
- Zhang C (2005) Madden–Julian oscillation. *Rev Geophys* 43:RG2003. doi:[10.1029/2004RG000158](https://doi.org/10.1029/2004RG000158)